Dynamics of Atmospheres and Oceans 72 (2015) 88–101

Contents lists available at ScienceDirect

Dynamics of Atmospheres and Oceans

journal homepage: www.elsevier.com/locate/dynatmoce

Madden–Julian Oscillation simulated in BCC climate models

Chongbo Zhao, Hong-Li Ren*, Lianchun Song, Jie Wu

Laboratory for Climate Studies, National Climate Center, China Meteorological Administration, 46 Zhongguancun Nandajie, Haidian District, Beijing 100081, China

ARTICLE INFO

Article history:
Received 26 May 2015
Received in revised form 2 October 2015
Accepted 23 October 2015
Available online 30 October 2015

Keywords:
Madden–Julian Oscillation
BCC
AMIP
Historical

ABSTRACT

This study evaluates the ability of four versions BCC (Beijing Climate Center or National Climate Center) models (BCC_AGCM2.1, BCC_AGCM2.2, BCC_CSM1.1 and BCC_CSM1.1m) in simulating the MJO phenomenon using the outputs of the AMIP (Atmospheric Model Intercomparison Project) and historical runs. In general, the models can simulate some major characteristics of the MJO, such as the intensity, the periodicity, the propagation, and the temporal/spatial evolution of the MJO signals in the tropics. There are still some biases between the models and the observation/reanalysis data, such as the overestimated total intraseasonal variability, but underestimated MJO intensity, shorter significant periodicity, and excessive westward propagation. The differences in the ability of simulating the MJO between AMIP and historical experiments are also significant. Compared to the AMIP runs, the total intraseasonal variability is reduced and more realistic, however the ratio between the MJO and its westward counterpart decreases in the historical runs. This unrealistic simulation of the zonal propagation might have been associated with the greater mean precipitation over the Pacific and corresponded to the exaggeration of the South Pacific Convergence Zone structure in precipitation mean state. In contrast to the T42 versions, the improvement of model resolution demonstrate more elaborate topography, but the enhanced westward propagation signals over the Arabia Sea followed. The underestimated (overestimated) MJO variability over eastern Indian Ocean (Pacific) was assumed to be associated with the mean state. Three sets of sensitive experiments using BCC_CSM1.1m turn out to support this argument.

1. Introduction

Madden–Julian Oscillation (MJO) features an equatorially trapped and eastward propagated wave with a 30–80-day periodicity and planetary–scale circulation (Madden and Julian, 1971, 1972). The major MJO signals are located over the tropical eastern Indian Ocean and western Pacific, and its slow eastward propagation has an average speed of about 5 m s^{-1} (Weickmann et al., 1985; Knutson et al., 1986). The vertical structure of MJO is characterized by a boundary–layer moisture convergence preceding the major convection (Hendon and Liebmann, 1994; Maloney and Hartmann, 1998; Sperber, 2003; Hsu and Li, 2012; Zhao et al., 2013; Li, 2014). MJO, as its dominant role in contributing to the variability between day-to-day weather and El Nino–Southern Oscillation (ENSO), has been well known a major predictability source for the extended-range (10–30-day) forecasting (Li et al., 2015).

* Corresponding author. Tel.: +86 01068409514.
E-mail address: renhl@cma.gov.cn (H.-L. Ren).

http://dx.doi.org/10.1016/j.dynatmoce.2015.10.004

There are some considerable evidences for supporting the importance of MJO in influencing weather and climate variations over the tropics. For example, MJO has been known being intimately associated with the formation of tropical cyclones (Liebmann et al., 1994; Maloney and Hartmann, 2000; Higgins and Shi, 2001). MJO also interacts with ocean and thereby influences the evolution of ENSO (Takayabu et al., 1999; Kessler and Kleeman, 2000; Bergman et al., 2001). So far, the significant role of MJO in impacting the weather phenomena and climate systems has been widely recognized (Yang et al., 2012).

A realistic MJO simulation in model is the key for making a skillful prediction on the subseasonal–seasonal timescales. However, the ability of the most current climate models in predicting MJO is severely limited due to model misrepresentation of the MJO characteristics. Usually, the unrealistic features in the MJO simulations include weak amplitude, short period, fast eastward propagation and excessive westward propagation (Slingo et al., 1996; Annamalai and Sperber, 2005; Lin et al., 2006; Zhao et al., 2014). Accordingly, problems in MJO modeling have been attributing to the inaccuracies in representation of the model resolution (Jia and Li, 2008), convective parameterization (Tokioka et al., 1988; Wang and Schlesinger, 1999), diabatic heating (Li et al., 2009), mean state (Ajayamohan and Goswami, 2007), and atmosphere–ocean interaction (Wang and Xie, 1998; Fu and Wang, 2004).

In this study, we will deeply examine the distinct roles of the model resolution and coupling through evaluating MJO as simulated in Beijing Climate Center climate system models (BCC_CSM1.1 and BCC_CSM1.1m) and their atmospheric general circulation models (BCC_AGCM2.1 and BCC_AGCM2.2) under the fifth phase of Climate Model Inter-comparison Project (CMIP5). In the second generation of BCC_AGCM, the parameterizations for the deep cumulus convection, dry adiabatic adjustment, latent heat and sensible heat fluxes over ocean surface, and snow cover fraction are replaced with new schemes (Wu et al., 2010). It is of particular interest to evaluate MJO simulations in this series of BCC climate models and examine the effects of both the model resolutions and atmosphere–ocean coupling on MJO simulation. Furthermore, such an evaluation is important for improving the simulation of MJO in the BCC models and helpful for developing the climate prediction system on the subseasonal–seasonal timescale.

The remaining parts of this paper are organized as follows. The models, data, methodologies, and experiments are introduced in Section 2. In Section 3 the performance of the models in simulating MJO are described, and in Section 4 the cause of the biases in the MJO simulations are discussed. Conclusions are given in Section 5.

2. Models description, validation data, and experiments design

2.1. Models description

There are four versions of BCC model used in the following analysis and diagnosis, including BCC_AGCM2.1, BCC_AGCM2.2, BCC_CSM1.1 and BCC_CSM1.1m. Respectively, BCC_AGCM2.1 and BCC_AGCM2.2 are used in the AMIP experiments, BCC_CSM1.1 and BCC_CSM1.1m are used in the historical experiments. The details can be found in http://forecast.bcccsm.ncc-cma.net/web/channel-11.htm.

BCC_AGCM2.1 is the version 2.1 of the Beijing Climate Center Atmospheric General Circulation Model developed at the National Climate Center (NCC), China Meteorological Administration (CMA), based on the community atmospheric model version 3 (CAM3) developed by the National Center for Atmospheric Research (NCAR), but uses a reference atmosphere can in dynamical core, which significantly improves the pressure gradient force calculation, regional and global performance, particularly for the tropospheric temperature and winds (Wu et al., 2008). New physical parameterizations also have been used to replace the primitive ones accordingly (Wu et al., 2010). For example, a new cumulus convective scheme has been implemented (Wu, 2012). BCC_AGCM2.1 is a spectral model with horizontal T42 truncation (∼2.8125°) and 26 layers in the vertical direction. BCC_AGCM2.2 is the latest version which is released as the atmospheric component of BCC_CSM1.1m. The motivation was to provide better resolved regional climate simulations when used in CMIP5 experiments. Compared with BCC_AGCM2.1, BCC_AGCM2.2 has a higher horizontal resolution T106 (∼1.125°) and some tunings have been done in the physics package at T106 resolution.

BCC_CSM1.1 is a climate system model in which the atmospheric component BCC_AGCM2.1, ocean component MOM4-L40 (Modular Ocean Model), land component BCC_AVIM1.0 (Atmosphere and Vegetation Interaction Model), and sea ice component SIS (Sea Ice Simulator) are adequately coupled and interact with each other through fluxes of momentum, energy, water and carbon at their interfaces (Xin et al., 2012). BCC_CSM1.1m is developed based on the BCC_CSM1.1 with a moderate resolution in the atmospheric component. The atmospheric component in BCC_CSM1.1m is the BCC_AGCM2.2 at T106 horizontal resolution and 26 vertical layers, and the land model is BCC_AVIM1.0 with a same horizontal resolution as the atmospheric model. The ocean component and sea ice component are still MOM4–L40 and SIS, with a different oceanic topography distribution from the BCC_CSM1.1. Both the ocean and sea ice model use a tripolar grid, in which the zonal resolution is 1° and the meridional resolution ranges from 1/3° to 1° poleward.

In AMIP experiments, the observed SST and sea ice temperature are served as the boundary forcing of numerical experiments. And the realistic forcing of greenhouse gas, solar constant and aerosol are also used to conduct standard AMIP runs from 1979 to 2008. The historical experiments perform the integration from 1850 to 2008, with realistic external forcing including greenhouse gas, solar radiation, ozone distribution, and aerosols. To facilitate the comparison with observational data, the 30-year results from 1979 to 2008 of the models are used in this study.

2.2. Validation data

To evaluate the models' performance in MJO simulation, the pentad-mean Climate Prediction Center (CPC) Merged Analysis of Precipitation (CMAP, Xie and Arkin, 1996) is used. The daily satellite-observed outgoing longwave radiation (OLR) observed from the Advanced Very High Resolution Radiometer (AVHRR) on board National Oceanic and Atmospheric Administration (NOAA) satellites (Liebmann and Smith, 1996) and reanalysis wind field from the European Centre for Medium–Range Weather Forecast (ECMWF) reanalysis (ERA-Interim, Dee et al., 2011) are also used to evaluate the model performance. Prior to the analysis, the pentad–mean data are interpolated into daily values. We use the whole thirty years (from 1979 to 2008) data to validate the simulations and discuss the model biases. According to the metrics outlined by the U.S. CLIVAR (Climate Variability and Predictability) MJO working group, the 20–100-day band pass filter is used to isolate MJO component.

2.3. Experiments design

To test the effect of mean state varying in the MJO simulation, three additional sets of experiments using BCC_CSM1.1m are designed in this study. The first experiment (denoted as "CTL") is the same as the historical run during a period of 10 years. The second set of experiments (denoted as "CPN") involve reducing convective heating over the Central Pacific (CP), which is calculated from the dry static energy tendency in the convection scheme, by multiplying the factor ranges from 0 to 1. Thus precipitation is reduced over the CP. The third set of experiments (denoted as "IOP") involve increasing convective heating over the eastern Indian Ocean (IO) by multiplying the factor greater than 1. It leads to increased precipitation over the eastern IO. Comparing the results of CPN (IOP) with CTL, the effects of the mean state over the CP (eastern IO) on the MJO simulation can be measured.

3. MJO behavior

3.1. Intensity distribution, zonal propagation and significant period

We present an equatorial wavenumber-frequency diagram of the raw precipitation to isolate the characteristic spatial and temporal scales (Fig. 1). Consistent with previous results (Lin et al., 2010; Hung et al., 2013), the dominant spatial scale

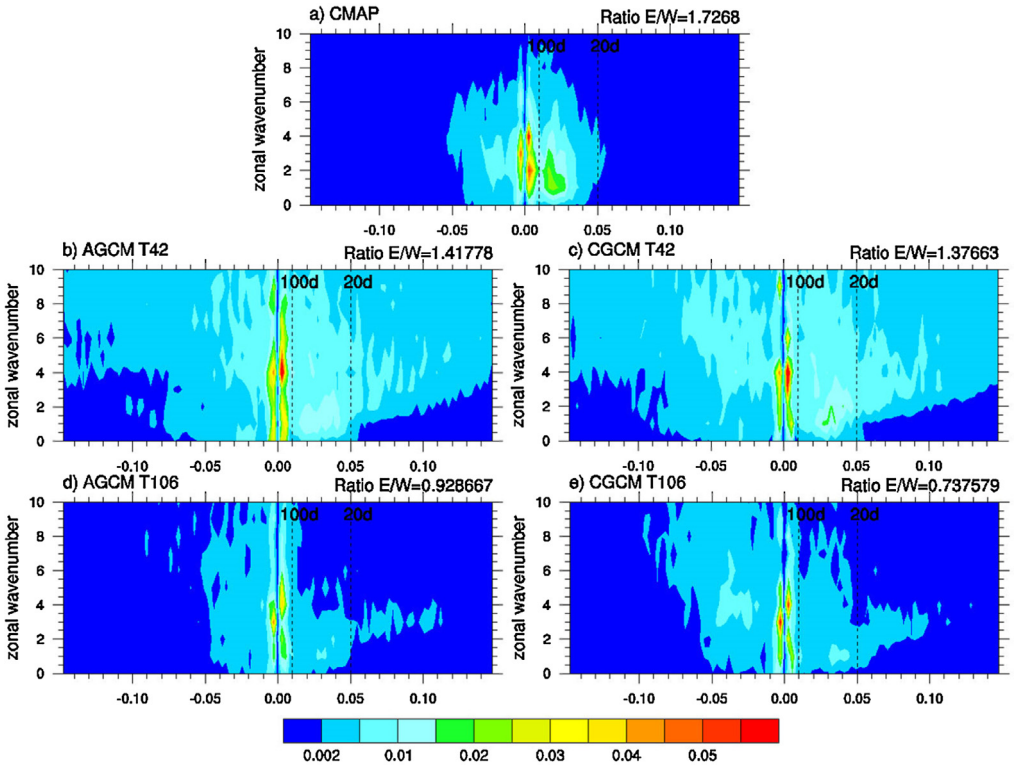

Fig. 1. Spectrum distribution of the eastward and westward propagating precipitation (averaged along 15°S–15°N) from CMAP, AMIP and historical run of BCC model with T42 and T106 horizontal resolution (unit: $mm^2\ day^{-2}$). Ratio between the MJO variance and the variance of its westward counterpart (wavenumber 0–10, 20–100-day mode) is labeled at top right of each panel.

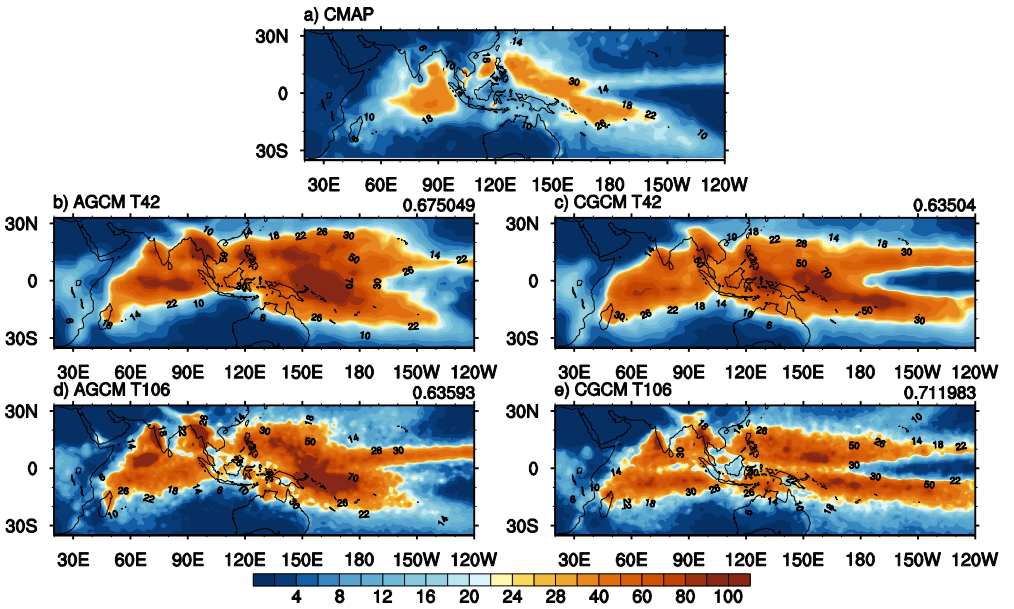

Fig. 2. Horizontal distribution of 20–100-day filtered precipitation variance of (a) CMAP, (b–c) AMIP and historical run of BCC model with T42 horizontal resolution, (d–e) AMIP and historical run of BCC model with T106 horizontal resolution (unit: $mm^2\ day^{-2}$) during 1979–2008. The pattern correlations between models and CMAP are marked at the top–right corner of each panel.

is zonal wavenumbers 1–3 for intraseasonal precipitation in the observation (Fig. 1a). For the wavenumber 1–3, the highest intraseasonal spectrum energy (with a value of about 0.02 $mm^2\ day^{-2}$) appears at the period of 60 days. The intraseasonal eastward propagating power tends to be concentrated on a higher frequency (a period around 30 days) in the BCC models. In AMIP runs (Fig. 1b and d), the zonal wavenumber 1 of intraseasonal precipitation is captured to a certain extent by the models, however, the intensity is evidently underestimated. As shown in Fig. 1c and e, the westward spectral power is generally stronger in the historical run and this may be caused by the Rossby response to the overly heat source on the eastside of dateline over the Pacific.

To investigate the simulation skills of the intraseasonal precipitation magnitude and geographical distribution, we show the variance distribution of the 20–100-day band pass filtered precipitation (Fig. 2). The two major centers of the intraseasonal precipitation intensity are located over the tropical eastern Indian Ocean and western Pacific respectively, according to the observation (Fig. 2a). Such two maximum centers can be approximately detected in both AMIP and historical runs of the models with T42 and T106 horizontal resolutions, but the amplitudes are generally overestimated in all the simulations. It is consist with the spectrum diagram that much more intraseasonal signals are situated on the smaller spatial scale (wavenumber greater than 5) in the models. The maximum center of variance shifts westward over the Indian Ocean and extends eastward over south western Pacific in historical runs. Compared with the AMIP runs, the amplitudes of the variance maxima are obviously reduced and more realistic in the historical runs. Especially the highest pattern correlations (around 0.71) between model and CMAP appears in the T106 version, indicating a higher skill due to the higher resolution.

Additionally, MJO dynamics essentially involve the complex interactions between convection and large-scale circulation, and thus RMM (Real-time Multivariate MJO series) indices (Wheeler and Hendon, 2004) are broadly used in the real-time MJO monitoring and prediction. Here, the structures of the two leading EOFs calculated from the combined intraseasonal OLR, U850, and U250 (due to the limitation of levels in the model output, U250 is used instead of U200) are presented in Fig. 3. EOF1 and EOF2 can totally explain 42% of the variance of the filtered atmospheric fields in the observation and reanalysis data (Fig. 3a). Of the two, EOF1 pattern exhibits the common situation of MJO with the enhanced convection (negative OLR anomalies) over the tropical Indian Ocean around 90°E nearby the Bay of Bengal, the upper-level easterly wind anomalies extending throughout the western Indian Ocean, and westerly wind anomalies over the Maritime Continent and western Pacific, while lower-level wind anomalies have the opposite zonal directions. EOF2 pattern has enhanced convection over the Maritime Continent and western Pacific Ocean, accompanied with the lower-level convergence and upper-level divergence. Lag correlations between PC1 and PC2 suggests the averaged 45-day period. In contrast, the first two EOFs of the AMIP simulations have explained less variance below 34% and the corresponding shorter period (around 32 days), which is consistent with Fig. 1. For the historical simulations, both the explained variance and significant period are less than those in the AMIP runs.

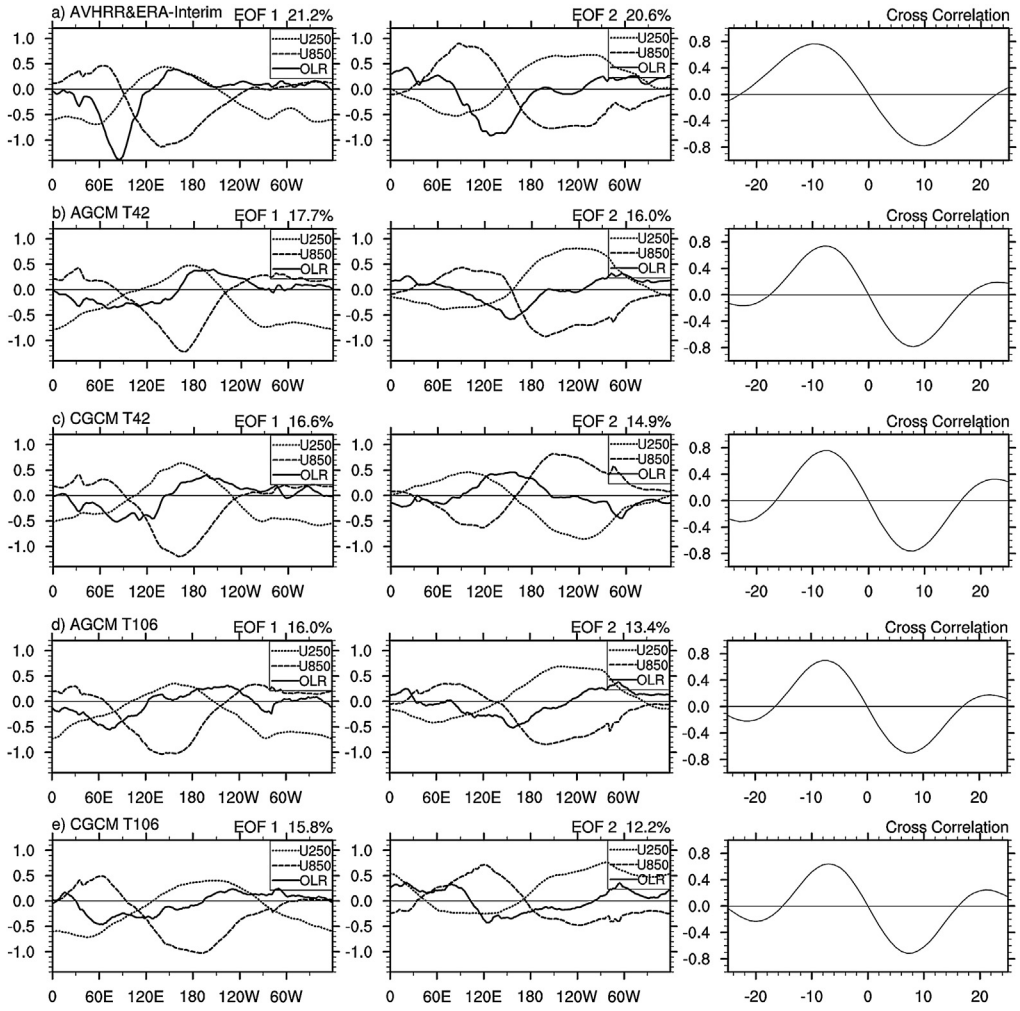

Fig. 3. Spatial structures of EOFs 1 and 2 of the combined analysis of OLR, u850, and u250 anomalies, and the cross correlation between PC1 and PC2 from (a) AVHRR and ERA–Interim, (b–c) AMIP and historical run of BCC model with T42 horizontal resolution, (d–e) AMIP and historical run of BCC model with T106 horizontal resolution.

3.2. Horizontal and vertical evolution

Many previous studies have noted the continuously eastward propagation of MJO along the equator. To estimate the eastward propagation speed, Fig. 4 shows the lag correlation coefficients between filtered OLR and PC1 (left column), and the regressed OLR anomalies with respect to PC1 (right column). Following the approach of Ling et al. (2014), on this time-longitude diagram of filtered OLR with respect to PC1, a set of straight lines can be drawn within a given longitudinal sector (listed in Table 1), each with a slope at the minimum center on the western boundary. Among this set of lines, the one with the smallest averaged value represents the MJO convection track and the slope is defined as its eastward propagation speed. The typical speed is about 6 m s^{-1} over Indian Ocean and western Pacific in the observation data (Table 1) and the OLR anomalies propagate eastward faster along the equator in the Western Hemisphere than Eastern Hemisphere. In models, the eastward propagation speeds of intraseasonal signals are twice as observation. In the historical runs, MJO extends continuously towards the Western Hemisphere (around 120°W). Compared with the T42 models, the T106 model results (Fig. 4d and e) show a significant westward propagation with smaller spatial scales especially over the western Indian Ocean

Table 1
The eastward propagation speed in Fig. 4 which are calculated by the slopes between lagged days and longitude following Ling et al. (2014).

Observation/model	Observation	AGCM_T42	CGCM_T42	AGCM_T106	CGCM_T106
Longitudinal sector	45°E–180°E	45°E–135°W	45°E–135°W	45°E–135°W	45°E–135°W
Eastward propagation speed (m s^{-1})	6.21	14.50	11.60	12.42	13.38

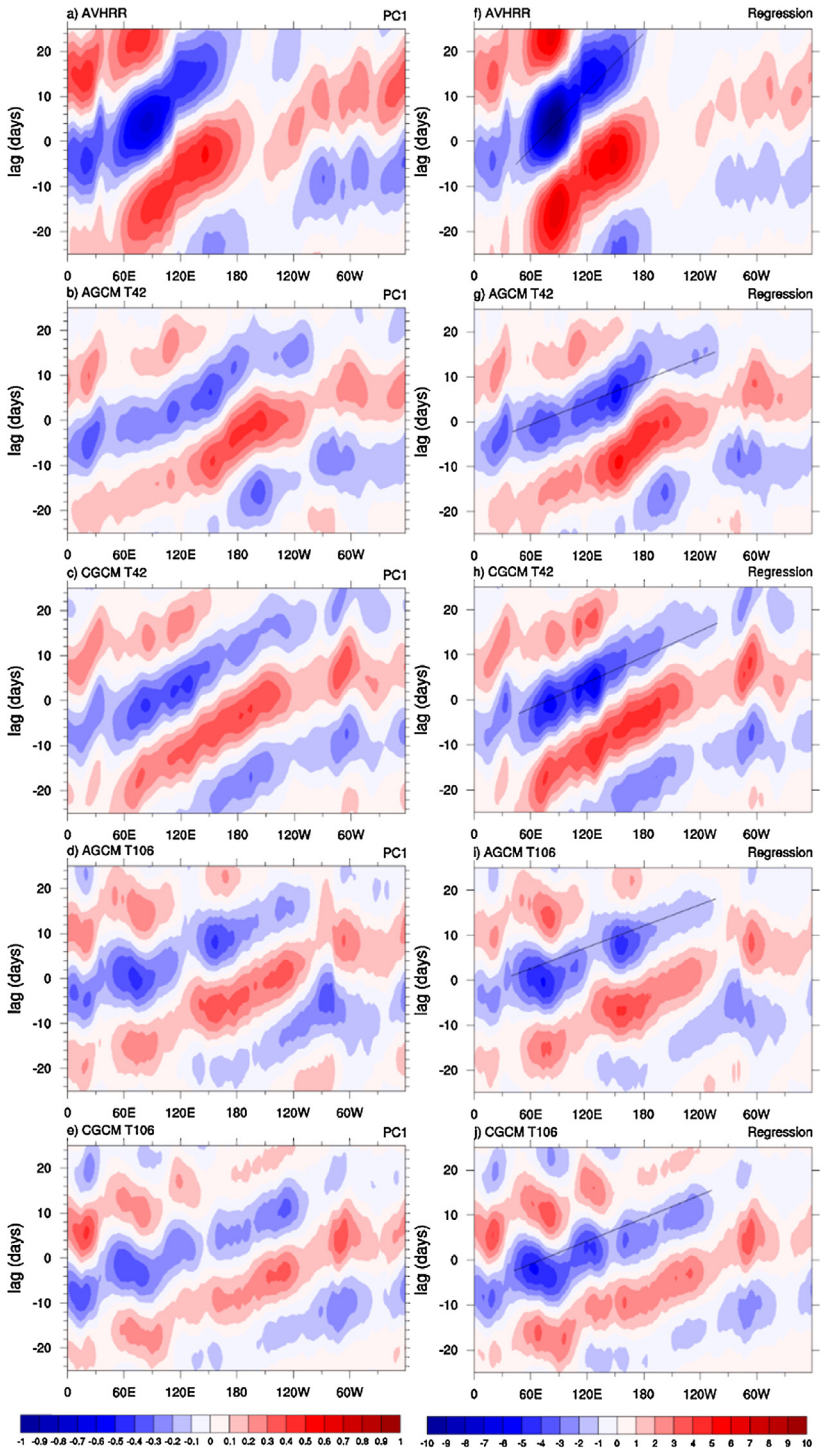

Fig. 4. Lag correlation coefficients between the 20–100-day band–pass filtered OLR averaged along 15°S–15°N and PC1 calculated in Fig. 3 (left panels), respectively, from (a) AVHRR, (b–e) AMIP and historical run of BCC model with T42 and T106 horizontal resolution. (f–j) are the same as (a–e), except for the regressed OLR anomalies onto PC1 (unit: W m^{-2}), the black lines represent the MJO convection track and the slopes are defined as their eastward propagation speed.

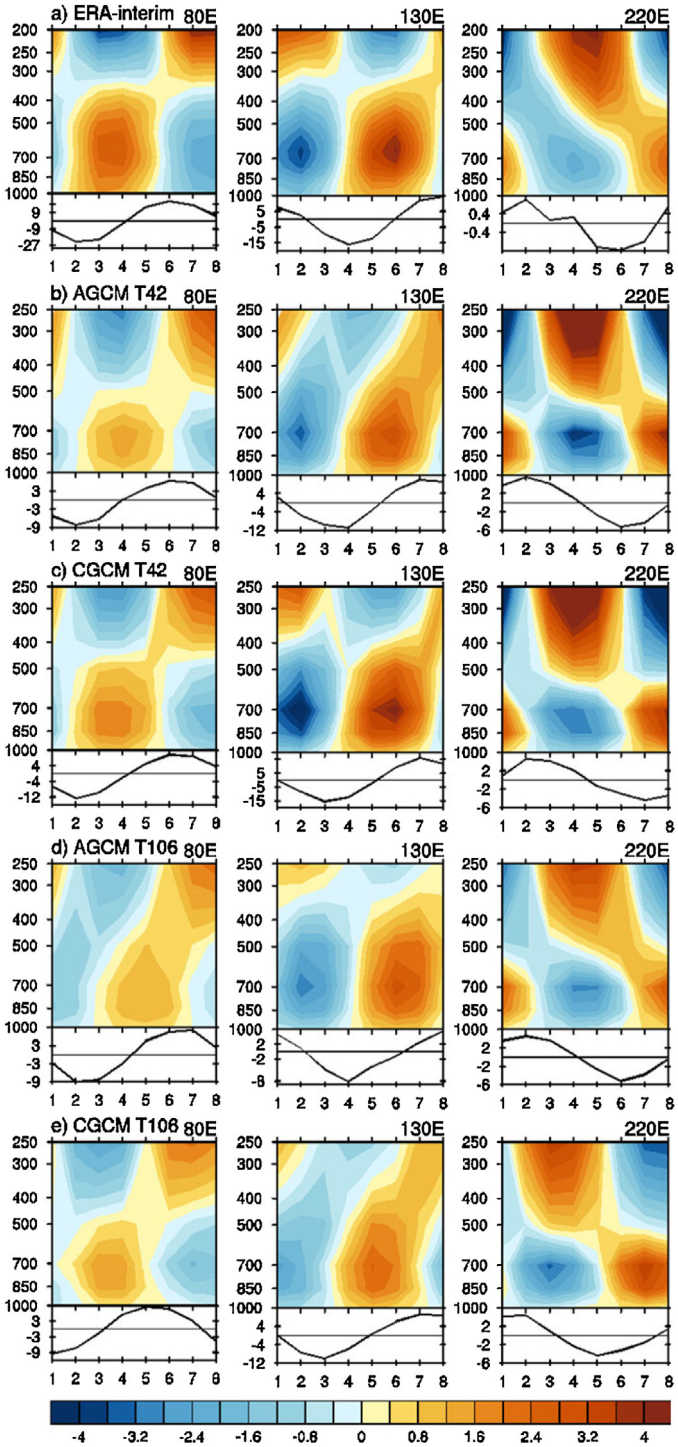

Fig. 5. Pressure-phase diagram of zonal wind anomalies (shaded) at three different longitudes 80°E (left), 130°E (middle) and 140°W (right) averaged between 15°S–15°N, respectively, in (a) ERA—Interim and AVHRR, (b–c) AMIP and historical run of BCC model with T42 horizontal resolution, (d–e) AMIP and historical run of BCC model with T106 horizontal resolution. Phases are defined according to PC1 and PC2 in Fig. 3. The units for zonal wind are m s^{-1}. OLR anomalies are plotted in lower panels (unit: W m^{-2}).

(50–80°E), implying that the higher resolution model with elaborate topography may lead to convection signals with smaller spatial scales. This is also consists with the greater intraseasonal variance over the Arabia Sea (Fig. 2).

Vertical structures of zonal wind and specific humidity are detected in both reanalysis and model data (Figs. 5 and 6), where the OLR anomalies are also plotted to show the convection evolution. Since phase 2 of MJO, the convection enhances

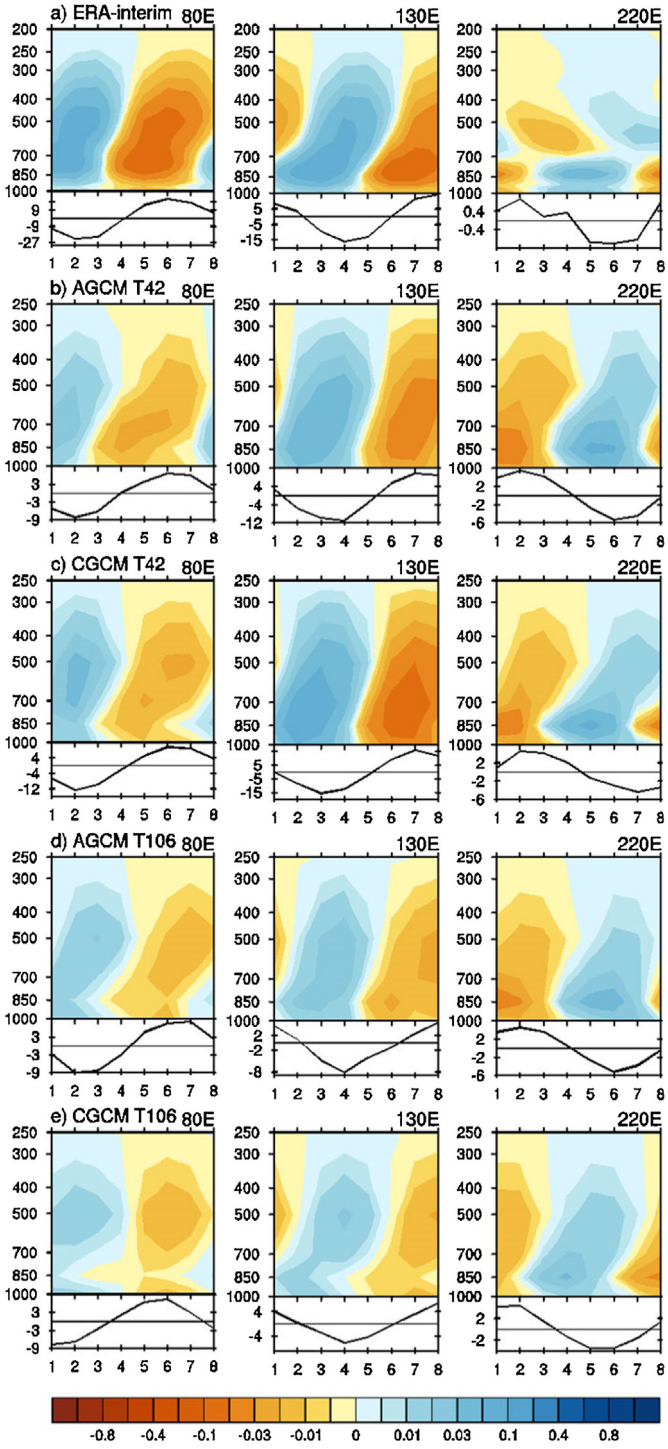

Fig. 6. Same as Fig. 5, except for specific humidity anomalies (unit: %).

gradually over the IO, accompanied with the zonal lower-level (upper-level) westerly (easterly) wind anomalies becoming stronger. Finally the zonal wind change into the opposite direction until phase 6. Much the same is true of western Pacific. Compared with the observation, the magnitude of zonal wind anomalies are stronger to the east of the dateline in the models. In the observation the maximum center of wind anomalies over the IO and western Pacific is located between 600 hPa and 700 hPa, whereas it is lower (700–850 hPa) in the models. Besides, the maximum westerlies over the IO in the models (3 m s^{-1}) are only 1/3 of that in the observation. The amplitudes of the maxima over the IO are slightly larger in the

historical runs than AMIP runs and closer to the observation. The moisture anomalies are also underestimated over IO and Pacific (Fig. 6). Thus, the convection formed under dryer circumstance consumes a lot of vapor, which is not conducive to the vertical transport of water vapor and the development of deep convection. Compared with the AMIP runs, the specific humidity is larger and closer to the reanalysis data in the historical runs. The simulated magnitude of specific humidity is also obviously related to the model resolution. The results from lower resolution models are closer to the reanalysis data.

4. Causes of the biases in MJO simulations

Fig. 7 shows the space-time spectra to further identify the signals of Kelvin, ER (equatorial Rossby), IG (intertio-gravity), MRG (mixed Rossby-gravity), and EIG (eastward intertio-gravity) modes in the tropics. The models can clearly reproduce the MJO as a significant signal. However, the signals of Kelvin (equatorial Rossby) wave are weaker (stronger) in both the historical and AMIP runs compared to the observation. This is consistent with Fig. 1 which shows that the ratio between the variances of MJO and its westward counterpart is significantly lower (less than 1.5) in the model results. Besides, compared with the AMIP runs, the spectrum energy of equatorial Rossby wave is even stronger in the historical runs. Thus, the westward propagation of equatorial intraseasonal signals is overestimated in the historical runs of BCC models. This bias may be caused by the overly heating source over the tropical central-eastern Pacific.

In the observation, the mean precipitation centers over the eastern IO and western Pacific (Fig. 8), and the total intraseasonal variance has a similar distribution (Fig. 2). The mean precipitation in the 4 BCC models have common biases over tropics: the underestimated intensity over the eastern IO and overestimated strength on the south side of equator over Pacific. Differences of mean surface temperature between the historical and AMIP runs are showed in Fig. 9. The atmosphere–ocean coupling yields the obvious warming biases on the south of the equator over the central–eastern Pacific. Generally speaking, SST warming enhances rainfall, while SST cooling depresses rainfall, without the feedback from atmosphere to ocean (Yang et al., 2012). In the historical runs, the surface temperature is higher nearby the Peru Coast accompanied by the extension

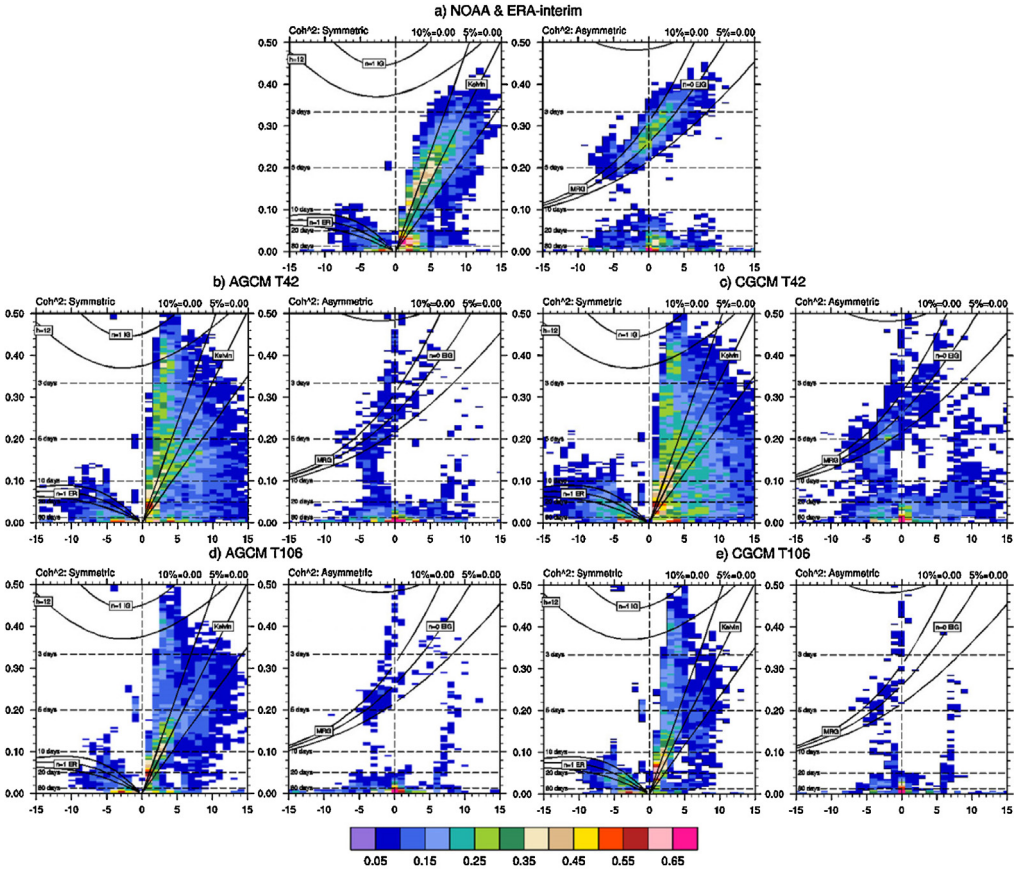

Fig. 7. The symmetric and asymmetric spectrum of coherence squared (color shading) between rainfall and U850, respectively in (a) AVHRR and ERA—Interim, (b–c) AMIP and historical run of BCC model with T42 horizontal resolution, (d–e) AMIP and historical run of BCC model with T106 horizontal resolution. Spectra were computed for individual latitudes before they were averaged over 15°S–15°N. Dispersion curves are shown for the Kelvin, equatorial Rossby (ER), intertio-gravity (IG), eastward intertio-gravity (EIG), and mixed Rossby-gravity (MRG) modes.

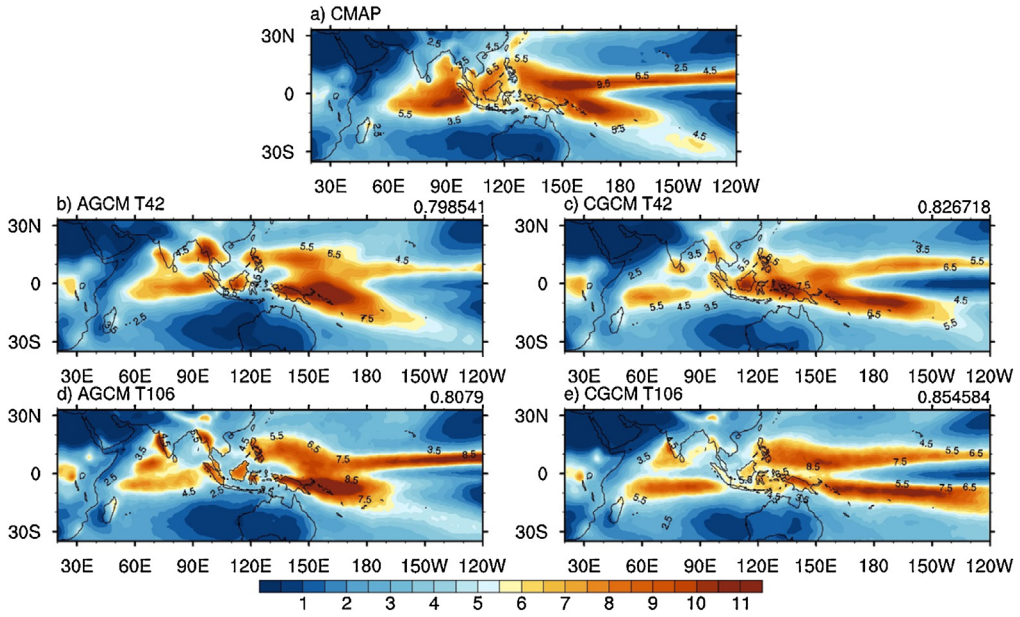

Fig. 8. Mean precipitation of (a) CMAP, (b–c) AMIP and historical run of BCC model with T42 horizontal resolution, (d–e) AMIP and historical run of BCC model with T106 horizontal resolution (unit: mm day^{-1}) during 1979–2008. The pattern correlations between models and CMAP are marked at the top-right corner of each panel.

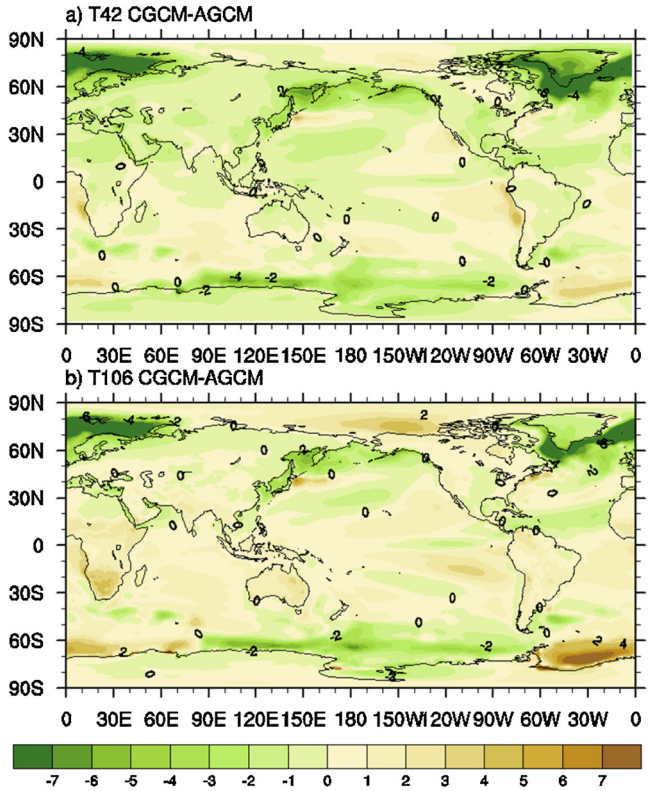

Fig. 9. Differences of mean surface temperature (unit: degree) between historical and AMIP runs of BCC model with (a) T42 and (b) T106 horizontal resolution.

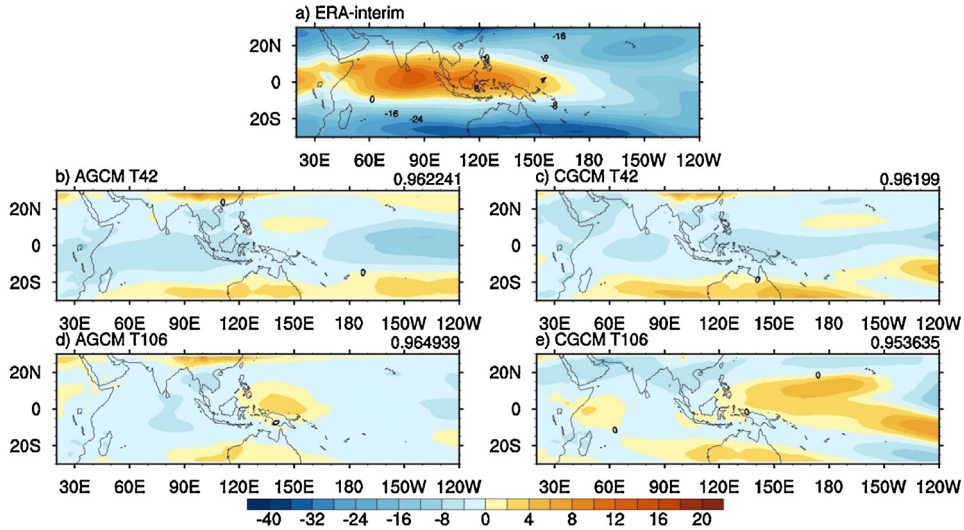

Fig. 10. Mean vertical shear (U_{850}–U_{250}) of (a) ERA—Interim during 1979–2008 and (b–e) the differences between 4 models and it (unit: m s^{-1}). The pattern correlations between models and ERA—Interim are marked at the top-right corner of each panel.

of south tropical convergence zone leading to warm and wet condition. Therefore, the biases in the mean precipitation are obviously enhanced on the south side of the equator over Pacific (Fig. 8).

Accompanied with the biases in mean precipitation, the zonal wind also have the similar bias distributions (Fig. 10). Previous studies indicate that mean easterly shear may have a great impact on the development of tropical perturbations (e.g., Wang and Xie, 1996; Sooraj et al., 2009; Pallav and Li, 2013). In ERA-Interim data, due to the strong easterlies at 250 hPa, the easterly shear over the precipitation centers (Fig. 10a) favors the development of intraseasonal oscillation. However, the associated weak easterlies at 250 hPa on the west of the less precipitation over the eastern IO in the models, lead to the weak easterly shear which suppresses the MJO convection over the IO (refer to Fig. 4f–j). In the historical run of T106 version,

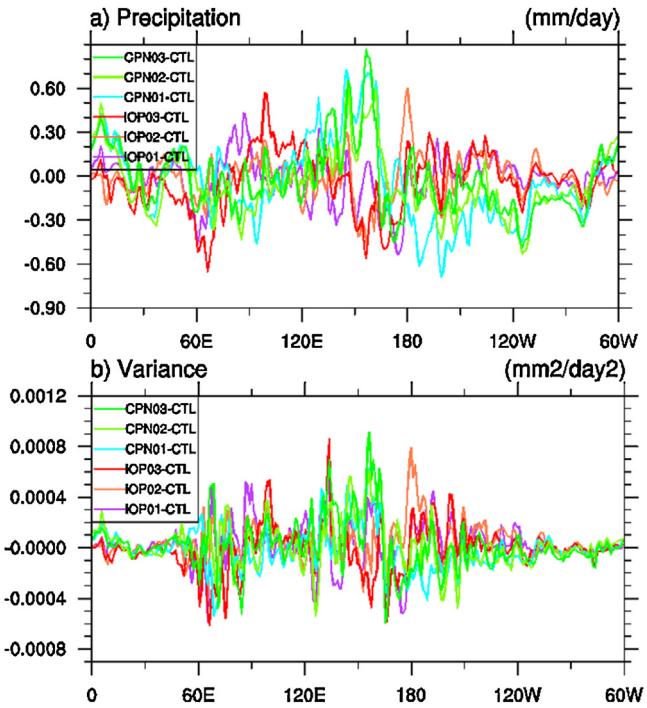

Fig. 11. (a) Mean precipitation differences along 15°S–15°N between sensitive experiments CPN01 (blue line), CPN02 (chartreuse line), CPN03 (green line), IOP01 (purple line), IOP02 (coral line), IOP03 (red line) and CTL run (unit: mm day^{-1}), (b) is the same as (a), except for the variance of 20–100-day filtered precipitation (unit: mm^2 day^{-2}).

Table 2
Experiment design.

Experiment	Description	Purpose
CTL	BCC–CSM1.1m, historical run	Provide reference for other experiments
CPN01	The convective heating over 20°S–0°N, 180°E–120°W are reduced by multiply 0.1	To reduce the role of the overly precipitation over CP on MJO simulation
CPN02	The convective heating over 30°S–0°N, 160°E–100°W are reduced by multiply 0.2	To reduce the role of the overly precipitation over CP on MJO simulation
CPN03	The convective heating over 20°S–0°N, 170°E–110°W are reduced by multiply 0.3	To reduce the role of the overly precipitation over CP on MJO simulation
IOP01	The convective heating over 15°S–15°N, 70°E–100°E are increased by multiply 2.0	To enhance the role of the weak precipitation over eastern IO on MJO simulation
IOP02	The convective heating over 10°S–0°N, 70°E–100°E are increased by multiply 3.0	To enhance the role of the weak precipitation over eastern IO on MJO simulation
IOP03	The convective heating over 15°S–15°N, 60°E–110°E are increased by multiply 5.0	To enhance the role of the weak precipitation over eastern IO on MJO simulation

the extended precipitation and easterly shear anomaly on the south side of the equator over Pacific (Fig. 10e) result in the eastward extended and strong intraseasonal signals over Pacific.

The above analysis indicates that the BCC model biases, i.e., the underestimated and westward shifted MJO over the IO, as well as the overestimated and eastward extended intraseasonal signals over Pacific, are associated with the local mean surface temperature, precipitation, and zonal wind. To further support this argument, three sets of sensitive experiments using BCC_CSM1.1m with T106 horizontal resolution are designed (Table 2). First, a 10-year integration is conducted from 1991 to 2000 in the historical run as control experiment ("CTL"). Second, to compare with the CTL run and reveal the role of the CP mean precipitation in effecting MJO activity, the convective heating over the CP region (20°S–0°N, 180°E–120°W;

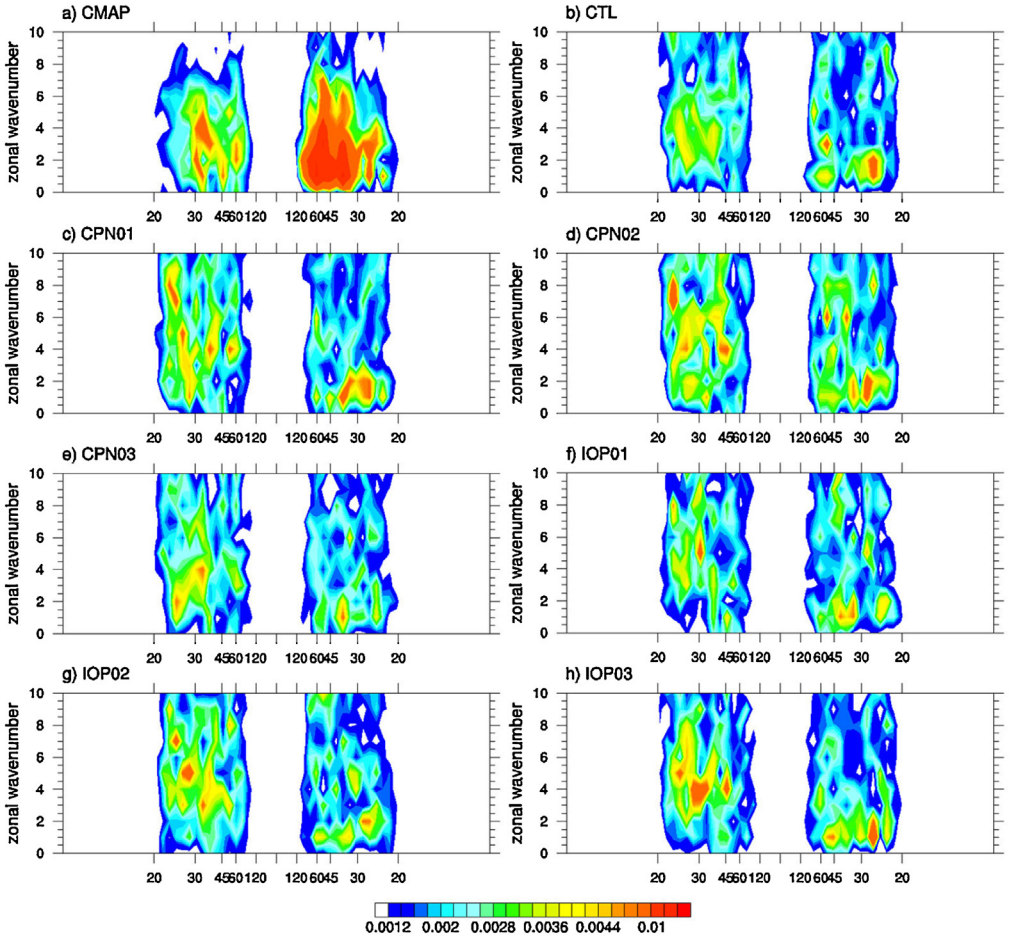

Fig. 12. Spectrum distribution (wavenumber from 0 to 10) of the 20–100-day filtered precipitation averaged along 15°S–15°N from (a) CMAP, (b) CTL, (c) CPN01, (d) CPN02, (e) CPN03, (f) IOP01, (g) IOP02 and (h) IOP03 run of BCC_CSM1.1m (unit: $mm^2\ day^{-2}$), the unit of the *x*-axis is day.

30°S–0°N, 160°E–100°W; 20°S–0°N, 170°E–110°W) are reduced by multiplying the factor (0.1, 0.2, 0.3). These are referred as "CPN" runs. Third, the convective heating over the IO region (15°S–15°N, 70°E–100°E; 10°S–0°N, 70°E–100°E; 15°S–15°N, 60°E–110°E) are increased by multiplying the factor (2.0, 3.0, 5.0) to enhance the mean precipitation over the eastern IO. These are referred as "IOP" runs. The difference of mean precipitation between the CPN (IOP) and CTL run is negative (positive) over the CP (IO) region (Fig. 11a), and the associated circulation may favor (against) the development of MJO. The total variance of intraseasonal precipitation varies similar with the mean precipitation (Fig. 11b), indicate the synchronization of mean state with MJO. Next, we will check whether the characteristics of MJO in the BCC_CSM1.1m are improved after decreasing (increasing) the mean precipitation over the tropical CP (eastern IO), respectively.

Compared with the CTL run, the precipitation anomalies show a consistent change in each experiment of the CPN (IOP) group. By reducing (increasing) the mean precipitation over the CP (eastern IO), the intraseasonal precipitation is enhanced (decreased) over eastern IO (CP), which is closer to the observation. Besides, although the spectrum power of eastward propagation component is still weak, the power below the 30-day period are significantly reduced and the 30–45-day period are effectively enhanced (Fig. 12c–h) on wavenumber 0–2. Therefore, a better mean state does act to cause a better depiction of MJO periods.

5. Conclusions

The skills in simulating the intraseasonal oscillation of the BCC models in 4 versions are evaluated in this study, focusing on the major characteristics of MJO, i.e., the intensity, periodicity, propagation, horizontal and vertical structure evolutions. It exhibits a certain capability in both the historical and AMIP runs of BCC models with T42 and T106 horizontal resolution, respectively. Compared with the observation and reanalysis data, the intraseasonal signals in the tropics can be reproduced relatively well in the model results. However, the simulated MJO still has some biases. These biases exhibit uniformity, including short period, weak intensity, fast eastward and significantly westward propagation, as well as less moisture during its lifecycle.

The improvement of model resolution demonstrates the topography better, but the enhanced westward propagation over the Arabia Sea followed. The historical runs displayed advantages in simulating reduced and realistic intraseasonal variability in the tropics. Although the warmer surface temperature over the central-eastern Pacific on the south side of the equator (Fig. 9) causes overly westward propagation turbulence like Rossby wave (Fig. 7). Therefore the less explained variance of MJO in the form of large scale deep convection eastward propagation appears in the coupled models.

Based on comparisons of the mean states including surface temperature, precipitation, and vertical shear of zonal wind, it has been found that the MJO simulation biases are associated with the deviations in the mean state simulation. We take the historical run of T106 model version as an example. The underestimated (overestimated) mean precipitation over the eastern IO (CP), accompanied with the weak (strong) easterlies at 250 hPa and suppressed (enhanced) easterly shear on the west side of the less (more) precipitation over the eastern IO (CP), can lead to the weak (strong) MJO signals over the IO (Pacific) in the models. To support this relationship between the mean state and MJO, three sets of sensitive experiments are performed. Results show that through increasing (reducing) the mean precipitation over the eastern IO (CP), the significant period of MJO can be evidently improved in the BCC_CSM1.1m model. The spectrum power of the MJO with zonal wavenumber 0–2 is significantly reduced at the period of less than 30 days and enhanced at the 30–45-day period. Therefore, a better depiction of MJO features necessarily needs a better reproduction of the mean state in the model.

Acknowledgements

This work is jointly supported by the National Basic Research program of China under grant 2015CB453203, the China Meteorological Special Program under grant GYHY201406022, the National Natural Science Foundation of China under grant 41375062 and 41505065, the China Postdoctoral Science Foundation funded project 2014M550677.

References

Ajayamohan, R.S., Goswami, B.N., 2007. Dependence of simulation of summer tropical intraseasonal oscillations on the simulation of seasonal mean. J. Atmos. Sci. 64, 460–478.
Annamalai, H., Sperber, K.R., 2005. Regional heat sources and the active and break phases of boreal summer intraseasonal (30–50 day) variability. J. Atmos. Sci. 62, 2726–2748.
Bergman, J.W., Hendon, H.H., Weickmann, K.M., 2001. Intraseasonal air–sea interactions at the onset of El Niño. J. Clim. 14, 1702–1719.
Dee, D., Coauthors, 2011. The ERA-Interim reanalysis: configuration and performance of the data assimilation system. Q. J. R. Meteorol. Soc. 137, 553–597.
Fu, X., Wang, B., 2004. Different solutions of intraseasonal oscillation exist in atmosphere ocean coupled model and atmosphere-only model. J. Clim. 17, 1263–1271.
Hendon, H.H., Liebmann, B., 1994. Organization of convection within the Madden–Julian Oscillation. J. Geophys. Res. 99, 8073–8083.
Higgins, W., Shi, W., 2001. Intercomparison of the principal modes of interannual and intra-seasonal variability of the North American monsoon system. J. Clim. 14, 403–417.
Hsu, P.C., Li, T., 2012. Role of the boundary layer moisture asymmetry in causing the eastward propagation of the Madden–Julian Oscillation. J. Clim. 25, 4914–4931.
Hung, M.P., Lin, J.L., Wang, W.Q., Kim, D., Shinoda, T., Weaver, S.J., 2013. MJO and convectively coupled equatorial waves simulated by CMIP5 climate models. J. Clim. 26, 6185–6214.
Jia, X.L., Li, C.Y., 2008. Impact of a GCM's resolution on MJO simulation. Adv. Atmos. Sci. 25, 139–156.
Kessler, W.S., Kleeman, R., 2000. Rectification of the Madden–Julian Oscillation into the ENSO cycle. J. Clim. 13, 3560–3575.

Knutson, R.R., Weickmann, K.M., Kutzbach, J.E., 1986. Global-scale intraseasonal oscillations of outgoing longwave radiation and 250 mb zonal wind during Northern Hemisphere summer. Mon. Weather Rev. 114, 605–623.
Li, C., Jia, X.L., Ling, J., Zhou, W., Zhang, C.D., 2009. Sensitivity of MJO simulations to diabatic heating profiles. Clim. Dyn. 32, 167–187.
Li, T., Zhao, C., Hsu, P.C., Nasuno, T., 2015. MJO initiation processes over the tropical Indian Ocean during DYNAMO/CINDY2011. J. Clim. 28, 2121–2135.
Li, T., 2014. Recent advance in understanding the dynamics of the Madden–Julian Oscillation. J. Meteorol. Res. 28, 1–33.
Liebmann, B., Smith, C.A., 1996. Description of a complete (interpolated) outgoing longwave radiation dataset. Bull. Amer. Meteorol. Soc. 77, 1275–1277.
Liebmann, B., Hendon, H.H., Glick, J.D., 1994. The relationship between tropical cyclone of the western Pacific and Indian Oceans and the Madden–Julian Oscillation. J. Meteorol. Soc. Jpn. 72, 401–411.
Lin, J.L., Kiladis, G.N., Mapes, B.E., Weickmann, K.M., Sperber, K.R., Lin, W., Wheeler, M.C., Schubert, S.D., Genio, A.D., Donner, L.J., Emori, S., Gueremy, J.F., Hourdin, F., Rasch, P.J., Roeckner, E., Scinocca, J.F., 2006. Tropical intraseasonal variability in 14 IPCC AR4 climate models, Part I: Convective signals. J. Clim. 19, 2665–2690.
Lin, J.L., Shinoda, T., Qian, T.T., Han, W.Q., Roundy, P., Zheng, Y.X., 2010. Intraseasonal variation of winter precipitation over the Western United States simulated by 14 IPCC AR4 coupled GCMs. J. Clim. 23, 3094–3119.
Ling, J., Bauer, P., Bechtold, P., Beljaars, A., Forbes, R., Vitart, F., Ulate, M., Zhang, C., 2014. Global vs. local MJO forecast skill of the ECMWF model during DYNAMO. Mon. Weather Rev. 142, 2228–2247.
Madden, R.A., Julian, P.R., 1971. Detection of a 40–50 day oscillation in the zonal wind in the tropical Pacific. J. Atmos. Sci. 28, 702–708.
Madden, R.A., Julian, P.R., 1972. Description of global-scale circulation cells in the tropics with a 40–50 day period. J. Atmos. Sci. 29, 1109–1123.
Maloney, E.D., Hartmann, D.L., 1998. Frictional moisture convergence in a composite life cycle of the Madden–Julian Oscillation. J. Clim. 11, 2387–2403.
Maloney, E.D., Hartmann, D.L., 2000. Modulation of eastern North Pacific hurricanes by the Madden–Julian Oscillation. J. Clim. 13, 1451–1460.
Pallav, R., Li, T., 2013. Relative roles of circumnavigating waves and extratropics on the MJO and its relationship with the mean state. J. Atmos. Sci. 70, 876–893.
Slingo, J.M., Sperber, K.R., Boyle, J.S., et al., 1996. Intraseasonal oscillation in 15 atmospheric general circulation models: results from an AMIP diagnostic subproject. J. Clim. Dyn. 12, 325–357.
Sooraj, K.P., Kim, D., Kug, J.S., Yeh, S.W., Jin, F.F., Kang, I.S., 2009. Effects of the low-frequency zonal wind variation on the high frequency atmospheric variability over the tropics. Clim. Dyn. 33, 495–507.
Sperber, K.R., 2003. Propagation and the vertical structure of the Madden–Julian Oscillation. Mon. Weather Rev. 131, 3018–3037.
Takayabu, Y.N., Iguchi, T., Kachi, M., Shibata, A., Kanzawa, H., 1999. Abrupt termination of the 1997–98 El Niño in response to a Madden–Julian Oscillation. Nature 402, 279–282.
Tokioka, T., Yamazaki, K., Kitoh, A., Ose, T., 1988. The equatorial 30–60 day oscillation and the Arakawa–Schubert penetrative cumulus parameterization. J. Meteorol. Soc. Jpn. 66, 883–901.
Wang, W.Q., Schlesinger, M.E., 1999. The dependence on convection parameterization of the tropical intraseasonal oscillation simulated by the UIUC 11-layer atmospheric GCM. J. Clim. 12, 1423–1457.
Wang, B., Xie, X., 1996. Low-frequency equatorial waves in vertically sheared zonal flow, Part I: stable waves. J. Atmos. Sci. 53, 449–467.
Wang, B., Xie, X., 1998. Coupled modes of the warm pool climate system, Part I: The role of air–sea interaction in maintaining Madden–Julian Oscillations. J. Clim. 8, 2116–2135.
Weickmann, K.M., Lussky, G.R., Kutzbach, J.E., 1985. Intraseasonal (30–60 day) fluctuations of outgoing longwave radiation and 250 mb stream function during northern winter. Mon. Weather Rev. 113, 941–961.
Wheeler, M., Hendon, H., 2004. An all-season real-time multivariate MJO index: development of an index for monitoring and prediction. Mon. Weather. Rev. 132, 1917–1932.
Wu, T.W., Yu, R.C., Zhang, F., 2008. A modified dynamic framework for atmospheric spectral model and its application. J. Atmos. Sci. 65, 2235–2253.
Wu, T.W., Yu, R.C., Zhang, F., et al., 2010. The Beijing climate center for atmospheric general circulation model (BCC AGCM 2.0.1): description and its performance for the present-day climate. Clim. Dyn. 34, 123–147.
Wu, T.W., 2012. A mass-flux cumulus parameterization scheme for large-scale models: description and test with observations. Clim. Dyn. 38, 725–744.
Xie, P., Arkin, P.A., 1996. Analyses of global monthly precipitation using gauge observations, satellite estimates, and numerical model predictions. J. Clim. 9, 840–858.
Xin, X., Wu, T., Zhang, J., 2012. Introductions to the CMIP 5 simulations conducted by the BCC climate system model (in Chinese). Adv. Clim. Change Res. 8, 378–382.
Yang, J., Bao, Q., Wang, X.C., Zhou, T.J., 2012. The tropical intraseasonal oscillation in SAMIL coupled and uncoupled general circulation models. Adv. Atmos. Sci. 29, 529–543.
Zhao, C., Li, T., Zhou, T., 2013. Precursor signals and processes associated with ISO initiation over the tropical Indian Ocean. J. Clim. 26, 291–307.
Zhao, C., Zhou, T., Song, L., Ren, H., 2014. The boreal summer intraseasonal oscillation simulated by 4 Chinese AGCMs participated in CMIP5 project. Adv. Atm. Sci. 31, 1167–1180.